Mixed-Mode I/II fracture behavior of asymmetric adhesively-bonded pultruded composite joints

CrossMark

Moslem Shahverdi, Anastasios P. Vassilopoulos *, Thomas Keller

Composite Construction Laboratory (CCLab), Ecole Polytechnique Fédérale de Lausanne (EPFL), Station 16, Bâtiment BP, CH-1015 Lausanne, Switzerland

A B S T R A C T

The mixed-mode fracture behavior of adhesively-bonded pultruded glass fiber-reinforced polymer joints was experimentally investigated using asymmetric mixed-mode bending specimens. The crack propagated along paths outside the symmetry plane and, therefore, mode partition could not be performed in the standardized way as for symmetric specimens. An approach based on the existing "global method", designated the "extended global method", was established and applied for the analysis of the experimental data and the fracture mode partitioning. Finite element models were developed in order to validate the approach. The virtual crack closure technique was used for calculation of the fracture components at the crack tip and an exponential traction–separation cohesive law was used to simulate the fiber bridging zone. In addition, the experimental compliance method was used for calculation of the fracture energy for the examined asymmetric mixed-mode bending specimens. Results obtained using the "extended global method" and the experimental compliance method were in good agreement with the results from FE models.

© 2013 Elsevier Ltd. All rights reserved.

1. Introduction

Adhesively-bonded joints are increasingly used as a joining technique for composite materials thanks to their better performance as a permanent connection compared to other joining techniques such as bolted joints [1]. Nonetheless, failure in such joints can occur due to crack propagation in the adherend along paths outside the symmetry plane [2]. In order to increase design reliability, the fracture behavior of such joints under mixed-Mode I/II loading must be carefully studied. The most commonly used specimen for the characterization of the mixed-Mode I/II fracture behavior of composite materials is the mixed-mode bending (MMB) specimen [3]. The MMB specimen proposed by Reeder and Crews [4] is a combination of the double cantilever beam (DCB) and the end notched flexure (ENF) specimen, both standardized specimens for measuring pure Mode I and Mode II interlaminar fracture respectively.

Almost any combination of Mode I and Mode II loading can be experimentally investigated by the MMB configuration [5–11]. The MMB specimen has been extensively used for the characterization of the mixed-mode fracture behavior of different composite materials such as thermoplastic and thermosetting carbon fiber composites [5], carbon/epoxy laminates [6], glass/epoxy composites [7,8], glass/vinylester composites [9], adhesively-bonded metal joints [10], and adhesively-bonded composite/composite joints [11].

The partitioning of the experimentally obtained total strain energy release rate, G_{tot}, into the G_I and G_{II} when mixed-mode conditions exist is challenging [12–18], especially in asymmetric specimens [12,13]. There are two analytical methods in the literature that can be used for mode partitioning: the "global method" based on beam theory [14], and the "local method"

---

* Corresponding author. Tel.: +41 216936393; fax: +41 216936240.
  E-mail address: anastasios.vasilopoulos@epfl.ch (A.P. Vassilopoulos).

Nomenclature

a	crack length
AMMB	asymmetric mixed-mode bending
B	specimen width
c, c_g	lever length and lever length to center of gravity
C, C_0	compliance and initial compliance
CSM	chopped strand mats
CZM	cohesive zone model
DCB	double cantilever beam
ECM	experimental compliance method
ENF	end notched flexure
EGM	extended global method
$(EI)_{eq}$	equivalent bending stiffness of joint
$(EI)_{eq1}, (EI)_{eq2}$	equivalent bending stiffness of upper arm and lower arm
ζ, η	local axes
FE	finite element
GFRP	glass fiber-reinforced polymer
G	strain energy release rate
G_I	G for Mode I
$G_{I\text{-}FE}, G_{I\text{-}EGM}$	G for Mode I from FE and from EGM
G_{II}	G for Mode II
$G_{II\text{-}FE}, G_{II\text{-}EGM}$	G for Mode II from FE and from EGM
G_{tip}	G at crack tip
G_{br}	G due to fiber bridging
G_{tot}	total G
h_1, h_2	specimen arm thicknesses
L	half-span length of AMMB specimen
l_{br}	fiber bridging length
m	slope of a plot of C versus a^3
MMB	mixed-mode bending
M_1, M_2	bending moment acting on upper and lower arm
M_I, M_{II}	bending moment corresponding to Mode I and II
P	applied load
P_g	weight of lever and attached apparatus
T_n, T_t	normal and tangential traction
VCCT	virtual crack closure technique
δ	crack opening displacement
δ_f	maximum crack opening displacement
$\delta_{f\text{-}n}$	maximum normal crack displacement
$\delta_{f\text{-}t}$	maximum tangential crack displacement
δ_n, δ_t	normal and tangential crack opening displacement
δ_P	load–point displacement
$\bar{\delta}$	opening displacement at maximum traction in cohesive model
$\bar{\delta}_n, \bar{\delta}_t$	normal and tangential opening displacement at σ_{max}
Δa	FE mesh size around the crack tip
σ_{max}	maximum traction
σ_{br}	fiber bridging traction in FE model
Φ	area under $\sigma-\delta$ curve that represents cohesive energy
ψ	ratio of equivalent bending stiffness of arms
ξ	ratio of equivalent bending stiffness of upper arm over equivalent joint stiffness

based on the stress intensity factor calculation around the crack tip [15]. According to the "global method" the mode partition is performed globally by including the whole region around the crack faces, whereas the "local method" considers only the "near-the-crack-tip" region as explained in [12,16]. Therefore, the "global method" is more appropriate for fracture analysis of materials that exhibit crack propagation accompanied by a large process zone, while the "local method" is more appropriate for materials with small fracture process zones, e.g. ceramics [12,16].

The mode partition can also be performed using FE models by means of the virtual crack closure technique (VCCT), see for example [19–22]. This method is quite accurate for calculation of the fracture energy at the crack tip, especially when homogenous materials are analyzed. However, when the crack path lies in a bi-material interface VCCT results concerning

mode partition become sensitive to the mesh size around the crack tip [23,24]. In order to overcome this problem, a method has been proposed by Atkinson [25] for analyzing isotropic fracture problems with a bi-material crack interface. This involves inserting a thin layer between the layers forming the interface and placing the crack within it. Because the crack tip is fully embedded in the resin layer, mode-mixity is not sensitive to mesh size.

Generally, the total fracture energy of a composite material comprises a fiber bridging component, G_{br}, and a tip component, G_{tip} [26]. The VCCT is able to calculate the fracture energy at the crack tip (G_{tip}). The fiber bridging zone can be considered as part of the fracture process zone where the fracture energy is released. Many efforts have been made to model the effects of fiber bridging, e.g. [26–30], and separate the two G components, mainly by finite element modeling, with the cohesive zone model approach being the most commonly used for determination of the G_{br}, see e.g. [26,27]. The behavior of the cohesive element is based on a traction–separation law that defines the stresses at a particular location in a prescribed cohesive zone as a function of the opening displacement of the zone at that location. Cohesive laws in FE modeling have been used extensively during recent years [26–30]. For example, the applicability of the CZM technique for modeling fiber bridging using a single layer of zero-thickness cohesive elements (COH2D4 in ABAQUS) along the delamination plane has been demonstrated by Sorensen et al. [26].

Although many researchers have studied the determination of the fracture behavior of composite materials under mixed-mode loading using symmetric and/or asymmetric MMB specimens, no studies exist in the literature regarding the experimental investigation and analysis of the fracture behavior of asymmetric MMB specimens comprised of orthotropic layered adherends. Neither does any study exist in which the effect of crack paths and fiber bridging on the fracture behavior of asymmetric MMB specimens is investigated.

The major objectives of the current study were the characterization of the mixed-mode fracture behavior of adhesively-bonded pultruded GFRP joints, the partitioning of the fracture mode components and the modeling of the fiber bridging that affects the total fracture energy. In such joints, the crack propagates along paths outside the symmetry plane where the materials on the two faces of the crack are different. In order to achieve these objectives, the crack propagation under different mixed-mode loading conditions in asymmetric MMB adhesively-bonded pultruded GFRP specimens was experimentally investigated. A new analytical method, based on the existing "global method" and designated the "extended global method", was introduced in order to analyze the experimental results and thus take the asymmetry effect into account. The virtual crack closure technique (VCCT) was used for calculation of the fracture components at the crack tip and a CZM was established for the simulation and quantification of the fiber bridging. The resulting *R*-curves obtained from FE models were compared to the experimental results analyzed by the experimental compliance method and the "extended global method".

2. Experimental investigation

2.1. Material description

Adhesively-bonded pultruded GFRP asymmetric MMB joints were examined under quasi-static loading. The laminates, supplied by Fiberline A/S, Denmark, consisted of E-glass fibers embedded in isophthalic polyester resin and had a width of 40 mm and thickness of 6.0 mm. The laminates, cut from I-beam profiles used for civil engineering applications, comprised two outer combined mat layers and a roving layer in the symmetry plane. One combined mat consisted of two outer chopped strand mats, CSM, and an inner woven 0°/90° fabric, all three stitched together. A 40-g/m² polyester surface veil was added on the outside. The fiber architecture of the laminates and corresponding thickness of each layer derived by optical microscopy are shown in Fig. 1. The fiber content, determined by burn-off tests in accordance with ASTM D3171-11 [31], was 43.2 vol.% based on the fiber density of 2560.0 kg/m³ specified by the manufacturer and the assumption that no voids were present; the fiber fractions are listed in Table 1. The weight of the second, inner combined mat was almost double that of the first, outer mat, and the proportion of woven fabrics was much higher. The longitudinal strength and Young's modulus of the
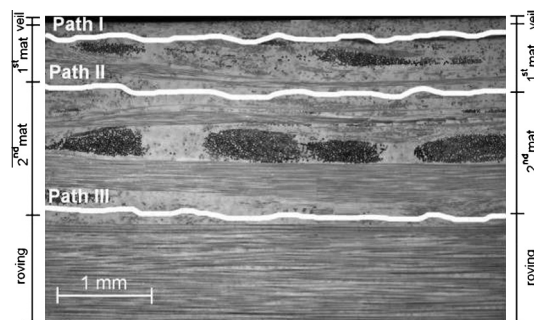

Fig. 1. Fiber architecture of upper half of a laminate (section parallel to pultrusion direction) and observed crack propagation paths.

Table 1
Fiber architecture and fractions by volume and weight of pultruded laminates.

Layers	Average thickness (mm)	% by vol.	% by weight
Veil	$2 \times 0.05^*$		
First combined mat	2×0.63		
– 2 CSM		2×1.7	2×2.5
– Woven 0°/90°		2×1.6	2×2.3
Second combined mat	2×1.07		
– 2 CSM		2×2.6	2×3.8
– Woven 0°/90°		2×4.1	2×6.0
Roving (UD)	1×2.5	1×23.3	1×34.2
Total	6.0	43.3	64.4

* "2×" = on each side of the symmetry axis.

GFRP laminate were obtained from tensile experiments, according to ASTM D3039/D3039M-08 [32], as being 307.5 MPa and 25.0 GPa respectively (average values from [2]).

A two-component epoxy adhesive system, Sikadur 330 supplied by Sika AG Switzerland, was used as the bonding material. The tensile strength of the adhesive was 39.0 MPa and the longitudinal Young's modulus 4.6 GPa (average value from [33]). The epoxy exhibited an almost elastic behavior and a brittle failure under quasi-static tensile loading.

2.2. Specimen description, set-up and procedure

A drawing and a photograph of the MMB configuration are shown in Figs. 2 and 3. The specimen length is 400 mm, and the half span length, L, is 170 mm, see Fig. 4. All surfaces subjected to bonding were mechanically abraded by approximately 0.3 mm to increase roughness and then chemically degreased using acetone. A Teflon film of 0.05-mm thickness, sufficiently thin for the given joints, was placed between the upper arm and the adhesive layer to introduce the pre-crack. The length of the pre-crack was a_0 = 50 mm measured from the loading line. The joint and the pre-crack lengths were selected with the aim to have long enough pre-crack length to achieve stable crack propagation, and enough overall joint length in order to reach a plateau in the R-curve. An aluminum frame was employed to assist the alignment of the two pultruded laminates during the fabrication. The 2-mm thickness of the adhesive was maintained by using spacers embedded in the bonding area. The resulting joints are representative for civil engineering structures where dimensions are significantly larger compared to aerospace or automotive applications. Typical adhesive thicknesses in such structures can vary significantly in order to compensate for tolerances.

In-house developed piano hinges were glued, using the same epoxy adhesive, at the end of both specimen arms to allow load application. After preparation of the configuration, the specimens were kept under laboratory conditions for 24 h and then placed for 24 h in a conditioning chamber at 35 °C and 50 ± 10% RH to ensure full curing of the adhesive. The resulting thickness of the MMB specimens was 13.4 mm and the pre-crack was located 1.0 mm above the center axis of the joints, see Fig. 4.

A 25-kN MTS Landmark servo-hydraulic testing rig, calibrated to 20% of its maximum capacity, was used for all the experiments conducted under laboratory conditions, 23 ± 5 °C and 50 ± 10% RH. The specimens were loaded under displacement control at a constant rate of 1 mm/min. The load was applied by means of a lever at a distance c from the fulcrum. The loading lever was an aluminum I-beam weighing 28.6 N, P_g, had a bending stiffness of around 170 times that of the MMB specimen and assumed to be rigid. The applied load, the mid-span load, and the left support reaction are applied via
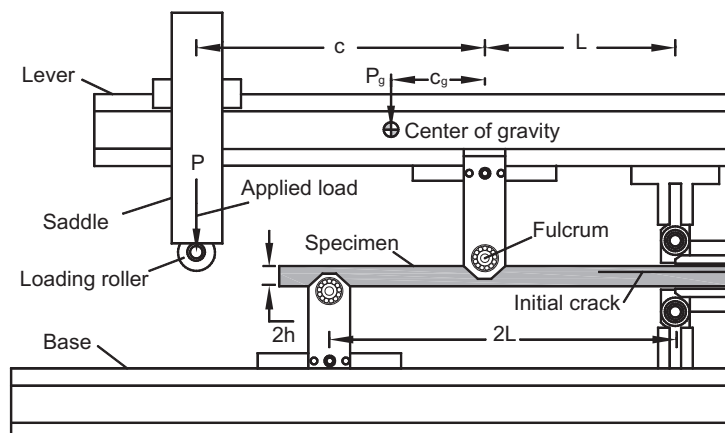
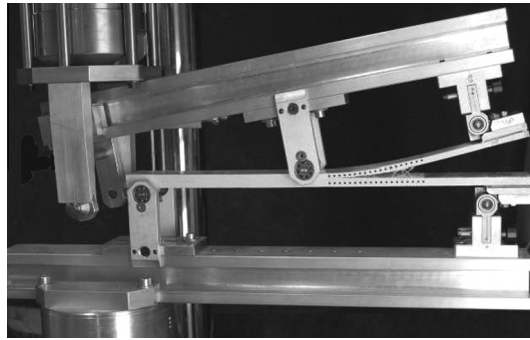

Fig. 2. Schematic of mixed-mode bending apparatus.

Fig. 3. Photograph of mixed-mode bending apparatus.
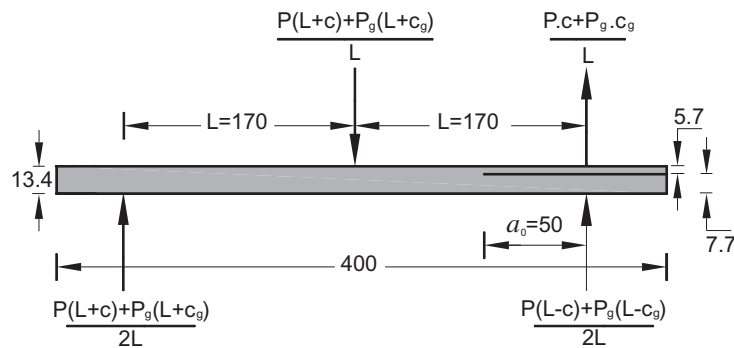

Fig. 4. Mixed-mode bending specimen with applied loads and dimensions in (mm).

bearing-mounted rollers to reduce the frictional force. The right end of the specimen is loaded using in-house developed piano hinges. The length of the loading lever, denoted c in Fig. 2, determines the mixed-mode ratio. The applied loads and displacements were continuously recorded. A total of 21 specimens with four different lever lengths, $c = 227, 150, 100$, and 60 mm, were examined, see Table 2.

The crack length was measured by means of a video extensometer. For this purpose pairs of black dots were marked at equal intervals of around 5 mm on the upper and lower lateral surfaces of the specimen, see Figs. 3 and 4. The X–Y coordinates of these dots were monitored by a video-extensometer camera and recorded continuously with a precision of 10^{-5} m by a Labview application. The crack length was determined based on the change in relative distance between each pair of

Table 2
MMB specimen geometrical parameters.

Specimen code	c (mm)	c_g (mm)
MMB-01	227	54
MMB-02	227	54
MMB-03	227	54
MMB-04	227	54
MMB-05	227	54
MMB-06	150	38
MMB-07	150	38
MMB-08	150	38
MMB-09	150	38
MMB-10	150	38
MMB-11	150	38
MMB-12	100	27
MMB-13	100	27
MMB-14	100	27
MMB-15	100	27
MMB-16	100	27
MMB-17	100	27
MMB-18	60	18
MMB-19	60	18
MMB-20	60	18
MMB-21	60	18

upper and lower black dots with a simple data processing module. According to this module, when the relative distance between each pair of black dots changed by more than 0.1 mm it was considered that the crack reached the position of these dots.

2.3. Experimental results

2.3.1. Observed failure modes

In all the examined specimens the observed failure mode, according to ASTM D 5573-99 [34], was a fiber-tear failure or light-fiber-tear failure, see Fig. 5. Fiber bridging started to develop with increasing crack opening displacement. Fibers from both arms of the specimen bridged the crack, transferring the load from one side to the other. At a certain crack opening displacement, fibers far from the crack tip were broken or pulled out, see crack length of up to around 85 mm in Fig. 5(e). The length along which fibers were not broken or pulled out is designated the "fiber bridging length", l_{br}, (crack length between 75 and 120 mm in Fig. 5(d)), and remained almost constant, following the crack tip for the rest of the fracture process, see Fig. 5(e) "crack length between 85 and 130 mm".

The pre-crack was located between the adhesive and first mat layer of the upper laminate, therefore the crack initiated and propagated along Path I, according to the nomenclature given in [2], see Fig. 1. However, in all the examined specimens, after a crack propagation of 5–20 mm the crack penetrated the first mat layer and propagated between the first and second mat layers corresponding to Path II. In some cases, the crack tip stopped propagating between the mat layers and a new crack appeared between the second mat layer and the roving layer, Path III. When this occurred, rovings of the woven fabric of the second mat layer bridged the two crack faces and significantly increased the applied load required for crack propagation. The term "roving bridging" was used in [2] to describe this phenomenon. According to the nomenclature used in [2] the crack path observed in this case was designated Path III with roving bridging. This phenomenon was observed in 11 of the 21 examined specimens.

2.3.2. Load–displacement responses

The load and crack length responses versus load–point displacement, δ_P, of representative specimens for a Path II crack under different lever lengths are shown in Figs. 6–9. Linear responses until crack initiation were observed in all cases. The slopes of the load–displacement curves in the linear part were 27.7, 48.5, 79.0, and 106.6 N/mm for c = 227, 150, 100, and 60 mm respectively. The load increased until a maximum value was reached and then gradually decreased. The maximum load obtained varied significantly when the lever length changed and increased as lever length decreased. The maximum load obtained from the representative specimen for c = 60 mm was around 1375 N, and was almost six times higher than that of the representative specimen for c = 227 mm, around 225 N.

As illustrated in Figs. 6–9, crack propagation was faster for lower lever lengths. For example, the crack length increment from 60 mm to 120 mm corresponded to around 17.0, 15.0, 6.0, and 2.5 mm displacement increment for c = 227, 150, 100,
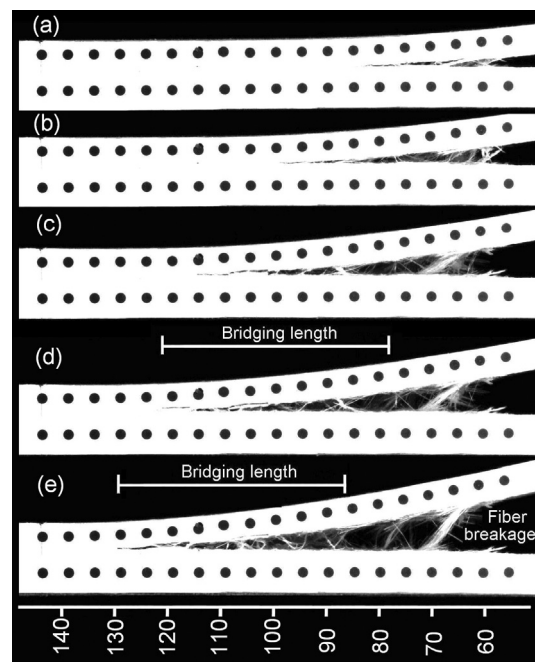
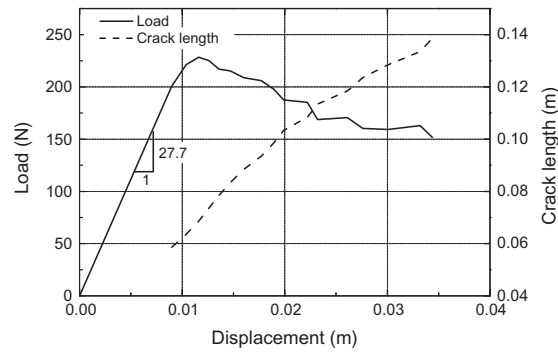**Fig. 5.** Side view of specimen MMB-02, dimensions in mm.

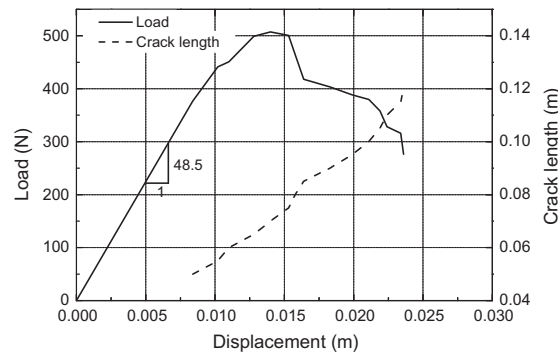**Fig. 6.** Load and crack length versus load–point displacement, MMB-04, c = 227 mm.

Fig. 7. Load and crack length versus load–point displacement, MMB-09, c = 150 mm.
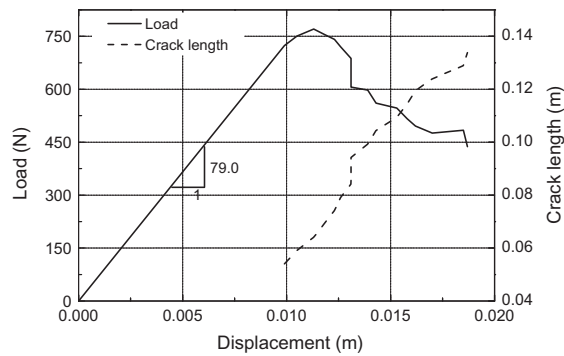

Fig. 8. Load and crack length versus load–point displacement, MMB-16, c = 100 mm.

and 60 mm respectively. In addition, with longer lever lengths the crack propagated steadily by displacement increment. However, with shorter lever lengths, unsteady crack propagation was observed; see Fig. 9 with a sudden crack length increase at around 17 mm.

3. Fracture data analysis

3.1. Experimental compliance method

The total strain energy release rate can be calculated by the experimental compliance method, ECM, based on experimentally derived values of loads, displacements, and crack lengths, as follows:
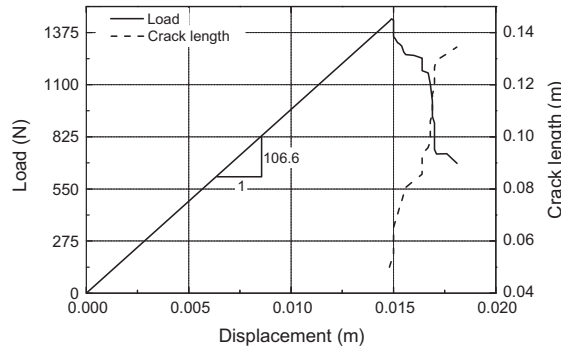
$$G = \frac{P^2}{2B} \frac{dC}{da} \tag{1}$$

Fig. 9. Load and crack length versus load–point displacement, MMB-19, c = 60 mm.

where P is the applied load, C is the compliance of the specimen, a is the crack length and B is the specimen width. The MMB specimen compliance is defined as:

$$C = \frac{\delta_P}{P} \tag{2}$$

where δ_P is the load–point displacement. From among different models for fitting compliance–crack length curves, Eq. (3) was selected because it better fits the experimental results according to [17]:

$$C = C_0 + ma^3 \tag{3}$$

The ECM method has also been used for mode partition in symmetric MMB specimens [4,17] where it is possible to determine the Modes I and II components of displacement along with the Modes I and II components of load, see [4] for details.

However, ECM cannot be used for the mode partitioning of mixed-mode results as is the case for the asymmetric and layered joint configurations used in this work. A new method designated the "extended global method", based on the "global method" [14], is therefore proposed in the next section for the mode partitioning of the examined specimens.

3.2. Extended global method

Williams [14] developed beam theory based equations for calculating the energy release rate from the values of bending moments and loads in a cracked laminate. In the present work, the equations have been modified in order to solve a crack propagation problem in which the crack is asymmetric and lies between two different orthotropic layers under the bending moments M_1 and M_2, as shown in Fig. 10. According to linear-elastic analysis, the total strain energy release rate is [16]:

$$G = \frac{6}{B^2} \left(\frac{M_1^2}{E_1 h_1^3} + \frac{M_2^2}{E_2 h_2^3} - \frac{(M_1 + M_2)^2}{E(h_1 + h_2)^3} \right) \tag{4}$$

where the bending moments (assumed positive when counterclockwise) are evaluated at a section of the specimen surrounding the crack tip. According to the "global method" [14] pure Mode I exists when symmetric moments act on the joint arms, i.e. $M_1 = M_I$ and $M_2 = -M_I$, and pure Mode II requires equal curvature of both arms, i.e. $M_1 = M_{II}$ and $M_2 = \psi M_{II}$. Furthermore, ψ is defined based on the ratio of the joint arm thicknesses h_1 and h_2. However, because the curvature of the orthotropic-layered arms depends on the bending stiffness rather than just the thickness, in the present work this definition is replaced by the equivalent bending stiffness ratio:

$$\psi = \frac{(EI)_{eq2}}{(EI)_{eq1}} \tag{5}$$

Therefore, under mixed-Mode I/II loadings are

$$M_1 = M_I + M_{II} \tag{6}$$

$$M_2 = -M_I + \psi M_{II} \tag{7}$$

Substitution of Eqs. (6) and (7) into Eq. (4) leads to the partition of G into G_I and G_{II} as:

$$G_I = \frac{M_I^2}{2B(EI)_{eq1}} \left(\frac{1 + \psi}{\psi} \right) \tag{8}$$

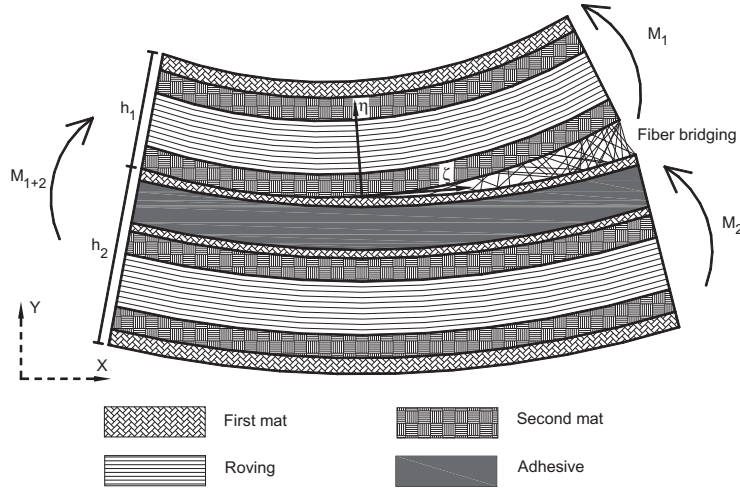$$G_{II} = \frac{M_{II}^2}{2B(EI)_{eq1}} \left(1 + \psi - \xi(1 + \psi)^2 \right) \tag{9}$$

Fig. 10. Schematic illustration of Path II crack in joint subject to bending moments.

with

$$\xi = \frac{(EI)_{eq1}}{(EI)_{eq}} \tag{10}$$

The ξ parameter, the ratio of the equivalent upper arm bending stiffness over the equivalent joint stiffness, like the ψ parameter, is defined as bending stiffness rather than thickness ratio. In the case of the asymmetric MMB specimen, as shown in Fig. 4, the bending moments at the section surrounding the crack tip are:

$$M_1 = \frac{Pc + P_g c_g}{L} a \tag{11}$$

$$M_2 = \frac{P(L - c) + P_g(L - c_g)}{2L} a \tag{12}$$

Substitution of Eqs. (11) and (12) into Eqs. (6) and (7) leads to:

$$M_I = \frac{(2\psi + 1)(Pc + P_g c_g) - (P + P_g)L}{2L(1 + \psi)} a \tag{13}$$

$$M_{II} = \frac{P(L + c) + P_g(L + c_g)}{2L(1 + \psi)} a \tag{14}$$

Substitution of Eqs. (13) and (14) into Eqs. (8) and (9) leads to:

$$G_I = \frac{[(2\psi + 1)(Pc + P_g c_g) - (P + P_g)L]^2}{8\psi\xi(1 + \psi)BL^2(EI)_{eq}} a^2 \tag{15}$$

$$G_{II} = \frac{[P(L + c) + P_g(L + c_g)]^2}{8\xi(1 + \psi)^2 BL^2(EI)_{eq}} (1 + \psi - \xi(1 + \psi)^2) a^2 \tag{16}$$

Eqs. (15) and (16) are closed form equations for the calculation of G_I and G_{II} in which all the parameters are obtained directly from the experiments.

3.3. Finite element method

2D plane-strain models were developed in ANSYS (academic version 13.0) to calculate the Modes I and II fracture components for different lever lengths (see Table 2). All layers of the laminates were modeled according to the thicknesses estimated by optical microscopy (see Table 1). The material properties are given in Table 3 and were adopted from [27]. The element PLANE182, a 4-node structural solid, was used to model different layers. A manual mesh with controlled mesh size was used. The aspect ratio of the elements in the vicinity of the crack tip was kept at 1/1 [20]. Elements of the same size were used on both sides of the crack tip to avoid any non-convergence that may be caused by different sizes. Nonlinear-elastic analysis was performed, allowing calculation of the specimen deformation, nodal forces and nodal displacements.

Table 3
Properties used for FE modeling.

Material data	First combined mat	Second combined mat	Roving	Veil	Adhesive
E_{11} (GPa)	12.8	15.1	38.9	3.2	4.6
E_{22} (GPa)	12.8	15.1	3.2	3.2	4.6
E_{33} (GPa)	3.2	3.2	3.2	3.2	4.6
G_{12} (GPa)	6.2	6.7	2.7	1.2	1.7
G_{23} (GPa)	1.4	1.4	1.4	1.2	1.7
G_{31} (GPa)	1.4	1.4	2.7	1.2	1.7
v_{12}	0.27	0.27	0.32	0.38	0.37
v_{23}	0.36	0.36	0.27	0.38	0.37
v_{31}	0.36	0.36	0.35	0.38	0.37
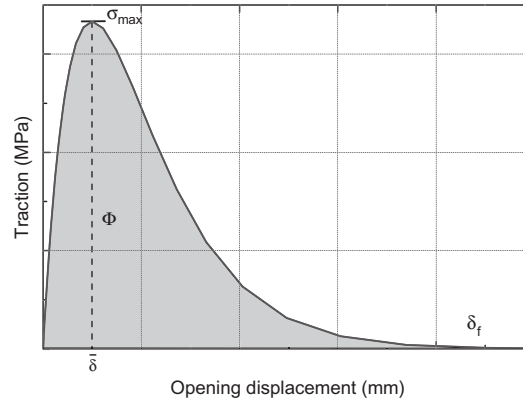
Fig. 11. Schematic illustration of cohesive traction–separation law.

Fiber bridging along the crack faces was modeled by using a single layer of zero-thickness cohesive elements, INTER202, along the crack plane. INTER202 is a 2-D 4-node interface element with two degrees of freedom at each node. The cohesive element behavior is based on a traction–separation law that defines the stresses, σ_{br}, at a particular location as a function of the opening displacement, δ. The traction–separation relationship is such that with increasing opening displacement the traction across the interface reaches a maximum, at $(\bar{\delta}, \sigma_{max})$, then decreases and eventually reaches zero, presenting a complete separation at an opening displacement of δ_f, at the end of the fiber bridging length, l_{br}, see Fig. 11. The length of the fiber bridging zone was obtained from the experimental observation. The area under the σ–δ curve represents the amount of energy dissipated during crack propagation in the cohesive zone, the cohesive energy. The three parameters cohesive energy, Φ, maximum traction, σ_{max}, and maximum opening displacement, δ_f, are interdependent and therefore the CZM can be described by two of them [35] assuming an appropriate traction–separation cohesive law model, which can be linear, polynomial, exponential or user-defined [26,28,29,36]. In this work, for modeling the fiber bridging, an exponential law was used, which according to [26] can model this effect better than the other laws. The applied exponential laws implemented in ANSYS software [36] and used in this work are following the assumption that the work of separation under pure shear and pure normal conditions are assumed to be equal to each other [35]. The normal and tangential tractions, T_n and T_t respectively are:

$$T_n = e\sigma_{max}\frac{\delta_n}{\bar{\delta}_n}e^{-\frac{\delta_n}{\bar{\delta}_n}}e^{-\left(\frac{\delta_t}{\bar{\delta}_t}\right)^2} \tag{17}$$

and

$$T_t = 2e\sigma_{max}\frac{\bar{\delta}_n}{\bar{\delta}_t}\frac{\delta_t}{\bar{\delta}_t}\left(1+\frac{\delta_n}{\bar{\delta}_n}\right)e^{-\frac{\delta_n}{\bar{\delta}_n}}e^{-\left(\frac{\delta_t}{\bar{\delta}_t}\right)^2} \tag{18}$$

where δ_n and δ_t are the normal and tangential opening displacements along the cohesive zone and $\bar{\delta}_n$ and $\bar{\delta}_t$ are the arbitrary normal and tangential opening displacements at maximum traction. The values of $\bar{\delta}$ and σ_{max} required by the CZM were estimated by an iterative procedure. The selected $\bar{\delta}$ is the one that allows the FE model to predict an opening displacement equal to δ_f, in which the traction reaches zero at the location of l_{br} behind the crack tip. Accordingly, selected σ_{max} values were those that resulted in the same loads computed by the FE models as those obtained from the experiments, for identical displacements and crack lengths. The estimated cohesive element model parameters for different lever lengths are listed in Table 4.

Table 4
Traction–separation cohesive model parameters for different lever lengths.

Specimen (lever length)	$\sigma_{\max}$ (MPa)	$\bar{\delta}_n$ (mm)	$\bar{\delta}_t$ (mm)
MMB-04 (c = 227 mm)	0.65	0.37	0.24
MMB-09 (c = 150 mm)	0.85	0.41	0.24
MMB-17 (c = 100 mm)	0.75	0.45	0.23
MMB-19 (c = 060 mm)	0.85	0.48	0.23
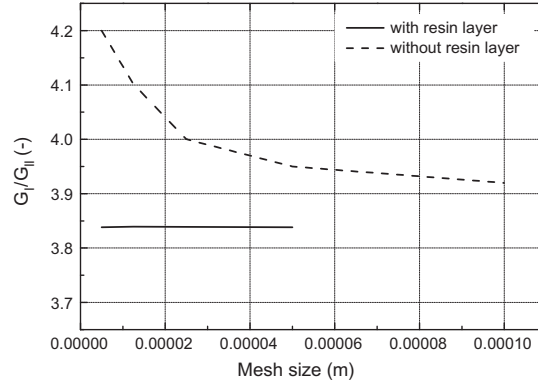
Fig. 12. Mesh sensitivity analysis for a crack along Path II, a = 100 and c = 227 mm.

The following equation represents the amount of energy dissipated in the crack-bridging zone, G_{br}, according to the CZM approach [26].

$$G_{br} = \int_0^{\delta_f} \sigma_{br} d\delta \tag{19}$$

where σ_{br} is the bridging traction and δ is the relative opening displacement along the fiber bridging length of the upper and lower arms. The G_{br} can be partitioned into Mode I and Mode II components as:

$$(G_{br})_I = \int_0^{\delta_{f-n}} (\sigma_{br})_\eta d\delta_\eta \tag{20}$$

and

$$(G_{br})_{II} = \int_0^{\delta_{f-t}} (\sigma_{br})_\zeta d\delta_\zeta \tag{21}$$

where δ_{f-n} is the maximum normal crack displacement, δ_{f-t} is the maximum tangential crack displacement, and ζ and η are the local axes, see Fig. 10. In Eqs. (19)–(21) the bridging traction is obtained from the cohesive elements in the FE models along the bridging length.
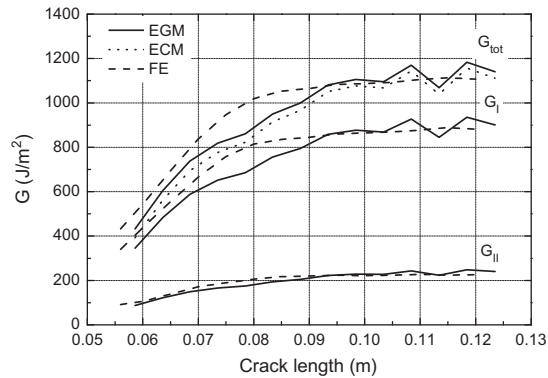
Fig. 13. *G* versus crack length from MMB-04 determined by extended global and experimental compliance methods and finite element modeling.
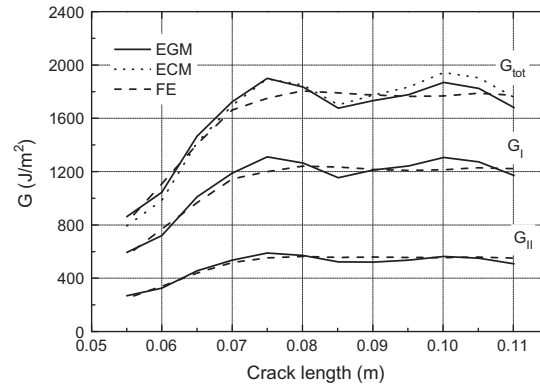
Fig. 14. *G* versus crack length from MMB-09 determined by extended global and experimental compliance methods and finite element modeling.
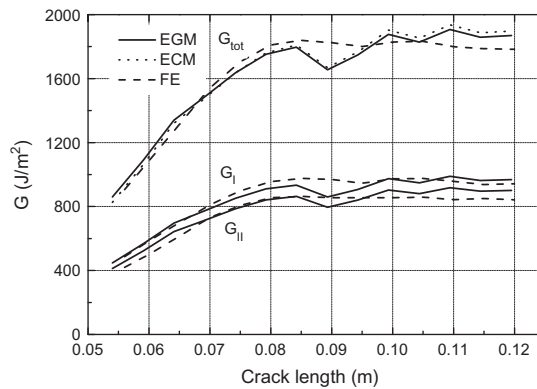

Fig. 15. *G* versus crack length from MMB-16 determined by extended global and experimental compliance methods and finite element modeling.
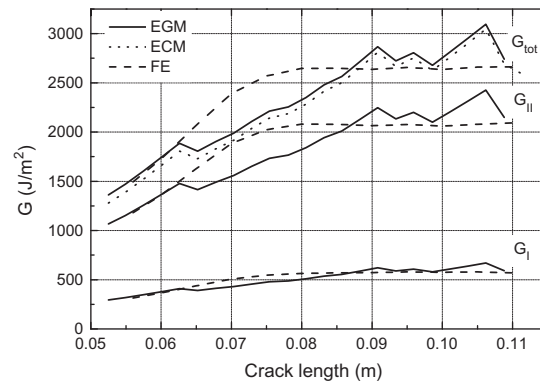

Fig. 16. *G* versus crack length from MMB-19 determined by extended global and experimental compliance methods and finite element modeling.

The VCCT was used for calculation of the fracture parameters at the crack tip. Bi-material interfaces were present in all specimens. Therefore, the calculated $G_{I\text{-tip}}$ and $G_{II\text{-tip}}$ components and the calculated mode-mixity, G_I/G_{II}, depended on the FE mesh size around the crack tip, Δa, and did not represent the actual fracture development, see the dashed line in Fig. 12. The approach proposed by Atkinson [25] was applied in [27] and in the present study in order to diminish the effect of the Δa. A thin "resin" interlayer was inserted which had the average properties of the adjacent layers of the interface. The thickness of the resin interlayer was selected as being 0.10 mm as a compromise resulting in almost no changes in the stiffness of the model (less than 1%) and also introducing a reasonable number of elements into the FE model. The mesh size was gradually varied from 0.050 mm to 0.005 mm, representing 2–20 elements through the resin interlayer. As shown in Fig. 12, the G_I/G_{II} component obtained for a Path II crack with a resin interlayer is independent of the mesh size.

Table 5
EGM strain energy release rate at different paths under different mixed-mode loading (J/m^2) with average values and standard deviations.

Specimen Code	Initiation				Path I				Path II				Path III				Roving bridging		
	G_I	G_{II}	G_{tot}	G_I/G_{II}	G_I	G_{II}	G_{tot}	G_I/G_{II}	G_I	G_{II}	G_{tot}	G_I/G_{II}	G_I	G_{II}	G_{tot}	G_I/G_{II}	G_I	G_{II}	G_{tot}
MMB-01	205	85	290	2.41					1061	287	1348	3.70	1024	144	1168	7.11			
MMB-02	166	69	235	2.41	410	151	561	2.71	963	260	1223	3.70							
MMB-03	133	55	188	4.41					837	226	1063	3.70					559	97	656
MMB-04	159	66	225	2.41					890	241	1131	3.70							
MMB-05	163	67	230	2.41	497	183	680	2.71	924	250	1174	3.70					424	74	498
Average	165 ± 26	68 ± 11	233 ± 36		454 ± 62	167 ± 23	620 ± 84		935 ± 84	253 ± 23	1188 ± 107		1024	144	1168		492 ± 95	86 ± 17	577 ± 112
MMB-06	162	128	290	1.27					851	387	1238	2.2	383	89	472	4.27	601	169	770
MMB-07	210	165	375	1.27	550	374	924	1.47	1247	567	1814	2.2					1156	326	1482
MMB-08	182	143	325	1.27	462	314	776	1.47	945	430	1375	2.2							
MMB-09	182	143	325	1.27					1190	541	1731	2.2							
MMB-10	181	143	324	1.27					1012	460	1472	2.2	700	164	864	4.27	800	225	1025
MMB-11	189	149	338	1.27	597	406	1003	1.47	1302	592	1894	2.2					1201	338	1539
Average	184 ± 16	145 ± 12	329 ± 28		536 ± 69	365 ± 47	901 ± 115		1091 ± 181	496 ± 82	1587 ± 263		542 ± 224	127 ± 52	668 ± 277		940 ± 288	265 ± 81	1204 ± 369
MMB-12	166	329	495	0.50	504	805	1309	0.63	1061	982	2043	1.08	921	366	1287	2.52	859	445	1304
MMB-13	149	296	445	0.50					776	719	1495	1.08							
MMB-14	118	235	353	0.50	351	560	911	0.63	918	850	1768	1.08							
MMB-15	167	331	498	0.50					975	903	1878	1.08					1073	556	1629
MMB-16	156	308	464	0.50	445	710	1155	0.63	1072	993	2065	1.08					331	172	503
MMB-17	170	337	507	0.50					921	853	1774	1.08							
Average	154 ± 19	306 ± 38	460 ± 58		433 ± 77	692 ± 124	1125 ± 201		954 ± 109	883 ± 101	1837 ± 211		921	366	1287		754 ± 382	391 ± 198	1145 ± 580
MMB-18	49	932	981	0.05	104	1126	1230	0.09	514	1836	2350	0.28							
MMB-19	45	852	897	0.05					616	2200	2816	0.28							
MMB-20	43	821	864	0.05	137	1484	1621	0.09	495	1768	2263	0.28	976	1041	2017	0.94	129	222	351
MMB-21	43	827	870	0.05					588	2100	2688	0.28					308	531	839
Average	45 ± 3	858 ± 51	903 ± 54		121 ± 23	1305 ± 253	1426 ± 276		553 ± 58	1976 ± 207	2529 ± 265		976	1041	2017		219 ± 127	377 ± 218	595 ± 345

The total strain energy release rates, G_{tot}, calculated by FE analysis were the sum of the G_{tip} and G_{br} under both Mode I and Mode II, i.e. $G_{tot} = (G_{tip})_I + (G_{tip})_{II} + (G_{br})_I + (G_{br})_{II}$. These values are compared with the obtained experimental ones in next section.

4. Results and discussions

The total strain energy release rate, G_{tot}, obtained by the experimental compliance method (ECM), the "extended global method" (EGM), and finite element (FE) modeling is illustrated in Figs. 13–16 for representative specimens of the four different mode-mixity ratios. Similar results were obtained from the three different methods with almost ideal R-curves. The mean value of the visually determined plateau – taking the typical scatter of this type of material into account – was assumed to represent the G_{tot} for propagation. The values of G_{tot} for the initiation and propagation based on EGM for all the specimens with the average values and standard deviations are presented in Table 5 according to the observed failure modes. In agreement with the results reported in [6–9,11], the total strain energy release rate corresponding to all paths increased as the lever length decreased, i.e. the Mode II contribution increased.

The mode partitioning results according to the "extended global method" and the non-linear FE analyses are also shown in Figs. 13–16. Similar mode partition was achieved using these two methods. The "extended global method" is more practical because it provides the fracture mode partition under mixed-mode loading conditions based on closed form equations with their parameters obtained directly from the experiments. In contrast, the use of the FE method requires the establishment of complex models containing parameters that must be estimated via iterative trial and error procedures. The mode-mixity obtained by the "extended global method" and the FE models for different lever lengths versus crack length are presented in Fig. 17. Slight variations of between 1% and 5% are observed between the two sets of results for lever lengths ranging from 227 to 60 mm. Nominal G_I/G_{II} ratios for Path II crack propagation corresponding to c = 227, 150, 100, and 60 mm were assumed to be 3.70, 2.20, 1.08, and 0.28 respectively, and are higher than the corresponding nominal values, 2.21, 1.02, 0.31, and 0.00, calculated according to ASTM D 6671-01 [3] by considering a symmetric joint configuration. Nominal G_I/G_{II} ratios for Paths I and III crack propagation are also presented in Table 5 with the values of G_I and G_{II} as a function of the associated crack paths for all specimens calculated by the "extended global method". The G_I/G_{II} ratios increased as
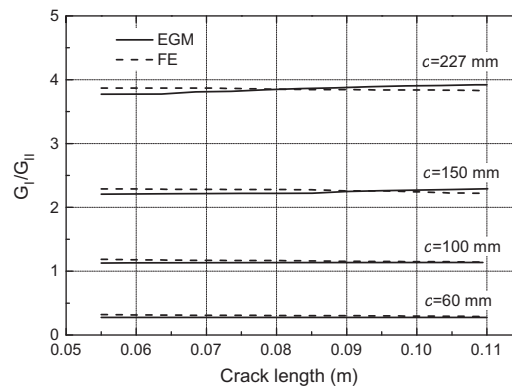
Fig. 17. Mode ratio, G_I/G_{II}, versus crack length determined by extended global method and finite element modeling.
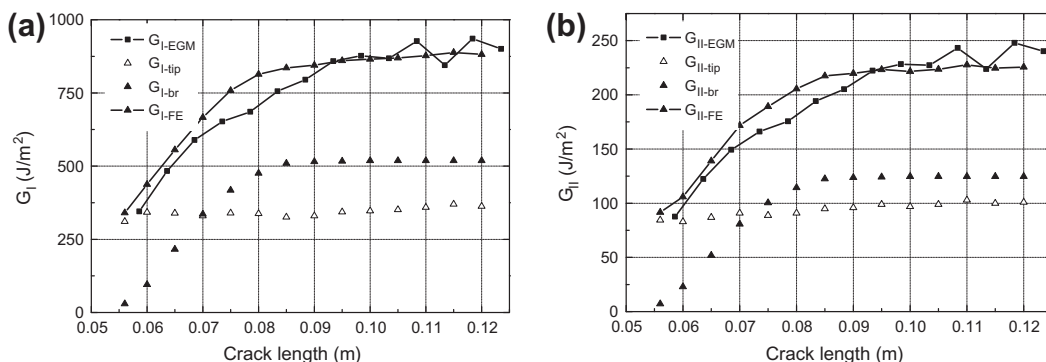
Fig. 18. Separation of G into G_{tip} and G_{br}, MMB-04 (c = 227 mm), (a) G_I and (b) G_{II}.
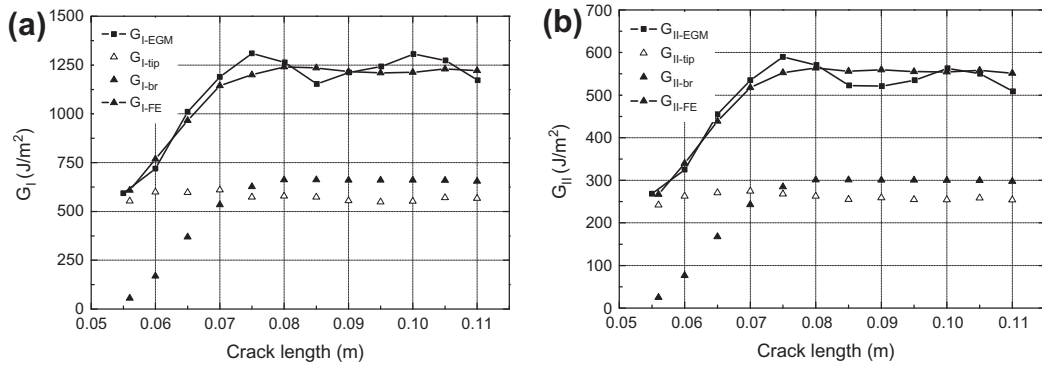
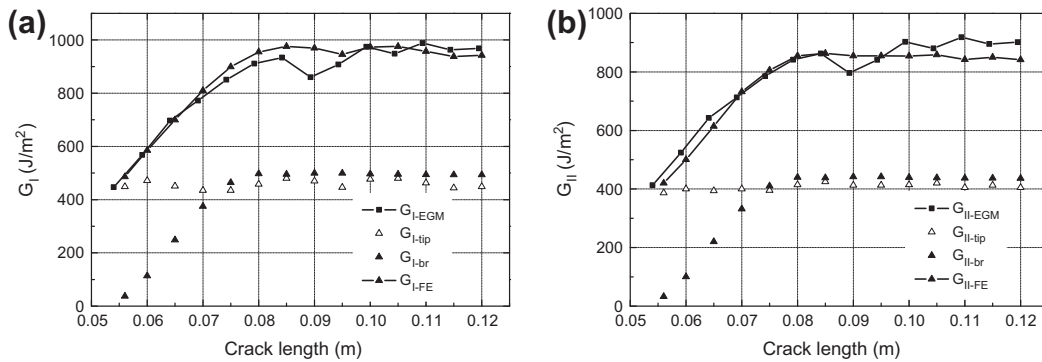**Fig. 19.** Separation of G into G_{tip} and G_{br}, MMB-09 (c = 150 mm), (a) G_I and (b) G_{II}.

Fig. 20. Separation of G into G_{tip} and G_{br}, MMB-16 (c = 100 mm), (a) G_I and (b) G_{II}.
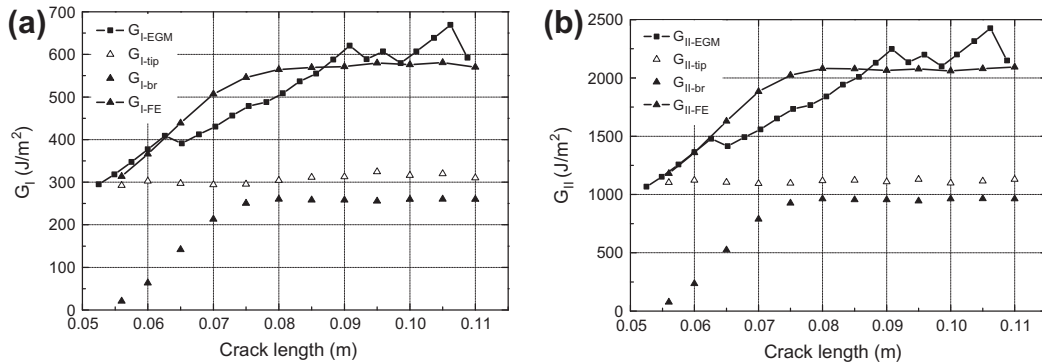

Fig. 21. Separation of G into G_{tip} and G_{br}, MMB-19 (c = 60 mm), (a) G_I and (b) G_{II}.

the crack propagated in a deeper path. The average values with standard deviations for the four different configurations are also given in this table.

The G_I and G_{II} curves shown in Figs. 13–16 for different mode-mixity ratios are expressed as the sum of the energy release rate at the crack tip, G_{tip}, and the contribution of the fiber bridging, G_{br}, in Figs. 18–21. Fiber bridging results in an increase of G with increasing crack length. This phenomenon is expressed by the R-curve that follows an initially increasing trend before reaching a plateau as from which the bridging length remains constant. Using the presented FE models, it was possible to compute the G_{tip} and G_{br} for the representative specimens. The summation of these two values, shown as "G_{I-FE} and G_{II-FE}" in Figs. 18–21, was in good agreement with the experimentally derived values according to the "extended global method". The contribution of the fiber bridging was not constant, depended on the G_I/G_{II} and decreased as the G_I/G_{II} decreased. The G_{br}/G ratio was around 60%, 55%, 52%, and 45% for MMB-04, MMB-09, MMB-17, and MMB-19 respectively.

5. Conclusions

The fracture behavior of 21 asymmetric MMB specimens composed of orthotropic, layered, pultruded GFRP laminate adherends and an epoxy adhesive was experimentally investigated. An "extended global method" in which the thickness ratios were extended to the bending stiffness ratios was used for the analysis of the experimental data and the mode partitioning. Finite element models were developed in order to validate the approach. Zero-thickness cohesive elements were used to model the fiber bridging zone. The following conclusions were drawn:

- The introduced "extended global method" is able to accurately determine the energy release rate and mode-mixity ratios from a set of closed form equations.
- Comparison of the G_{tot} values estimated/calculated according to the "extended global method", the experimental compliance method and FE modeling showed good agreement between the three approaches.
- FE models were used for the modeling of the fracture process. The bridging zone was modeled with cohesive elements and an exponential traction–separation law. The fiber bridging contribution decreased as G_I/G_{II} decreased.
- Analysis of the FE results showed that the mode-mixity ratios obtained from FE models is a function of the crack extension length when the crack propagates in a bi-material interface. Introduction of a resin interlayer with the average properties of the adjacent layers of the interface solved this problem.
- Cracks either propagated in one of the three crack paths defined in [2] (Path I between adhesive and 1st mat, Path II between 1st and 2nd mats or Path III between 2nd mat and roving layer) where fiber bridging occurred, or switched from Path II to Path III, thereby creating a roving bridge.

The results obtained from this study, combined with those for pure Mode I [2,27] and Mode II loading conditions (work in progress) can be used to establish initiation and propagation failure criteria which will prove invaluable for the design and analysis of such bonded composite joints for future structural applications.

Acknowledgments

References

[1] Vallee T. Adhesively bonded lap joints of pultruded GFRP shapes. PhD thesis, EPFL, Switzerland; 2004.
[2] Shahverdi M, Vassilopoulos AP, Keller T. A phenomenological analysis of Mode I fracture of adhesively-bonded pultruded GFRP joints. Engng Fract Mech 2011;78(10):2161–73.
[3] ASTM D 6671–01: Standard test method for mixed mode I–mode II interlaminar fracture toughness of unidirectional fiber reinforced polymer matrix composites. In: Annual book of ASTM standards, 15.03: 392–403.
[4] Reeder JR, Crews JR. Mixed-mode bending method for delamination testing. AIAA J 1990;28(7):1270–6.
[5] Kinloch AJ, Wang Y, Williams JG, Yayla P. The mixed-mode delamination of fibre composite materials. Compos Sci Technol 1993;47(3):225–37.
[6] Kim BW, Mayer AH. Influence of fiber direction and mixed-mode ration on delamination fracture toughness of carbon/epoxy laminates. Compos Sci Technol 2003;63(5):695–713.
[7] Benzeggagh ML, Kenane M. Measurement of mixed-mode delamination fracture toughness of unidirectional glass/epoxy composites with mixed-mode bending apparatus. Compos Sci Technol 1996;56(4):439–49.
[8] Ozdil F, Carlsson LA. Characterization of mixed mode delamination growth in glass/epoxy composite cylinders. J Compos Mater 2000;34(5):420–41.
[9] Dharmawan F, Simpson G, Herszberg I, John S. Mixed mode fracture toughness of GFRP composites. Compos Struct 2006;75(1–4):328–38.
[10] Liu Z, Gibson RF, Newaz GM. The use of a modified mixed mode bending test for characterization of mixed-mode fracture behavior of adhesively bonded metal joints. J Adhes 2002;78(3):223–44.
[11] Ducept F, Davies P, Gamby D. Mixed mode failure criteria for a glass/epoxy composite and an adhesively bonded composite/composite joint. Int J Adhes Adhes 2000;20(3):233–44.
[12] Harvey CM, Wang S. Experimental assessment of mixed-mode partition theories. Compos Struct 2012;94(6):2057–67.
[13] Ducept F, Gamby D, Davies P. A mixed-mode failure criterion derived from tests on symmetric and asymmetric specimens. Compos Sci Technol 1999;59(4):609–19.
[14] Williams JG. On the calculation of energy release rates for cracked laminates. Int J Fract 1988;36(2):101–19.
[15] Hutchinson JW, Suo Z. Mixed mode cracking in layered materials. Adv Appl Mech 1992;29(c):64–122.
[16] de Morais AB, Pereira AB. Mixed mode I + II interlaminar fracture of glass/epoxy multidirectional laminates – Part 1: Analysis. Compos Sci Technol 2006;66(13):1889–95.
[17] Bhashyan S, Davidson BD. Evaluation of data reduction methods for the mixed mode bending test. AIAA J 1997;35(3):546–52.
[18] Ozdil F, Carlsson LA. Beam analysis of angle-ply laminate mixed-mode bending specimens. Compos Sci Technol 1999;59(6):937–45.
[19] Rybicki EF, Kanninen MF. A finite element calculation of stress intensity factors by a modified crack closure integral. Engng Fract Mech 1977;9(4):931–8.
[20] Krueger R. The virtual crack closure technique: history, approach and applications. Appl Mech Rev 2004;57(2):109–43.
[21] Mathews MJ, Swanson SR. A numerical approach to separate the modes of fracture in interface crack propagation. J Compos Mater 2005;39(3):247–64.
[22] Silva A, de Freitas MJM. Mixed-mode delamination growth of laminar composite by using three-dimension finite element modeling. Fatigue Fract Engng Mater Struct 2003;26(6):543–9.
[23] Agrawal A, Karlsson AM. Obtaining mode mixity for a bimaterial interface crack using the virtual crack closure technique. Int J Fract 2006;141(1–2):75–98.
[24] Raju IS, Crews JH, Aminpour MA. Convergence of strain energy release rate components for edge delaminated composite materials. Engng Fract Mech 1988;30(3):383–96.
[25] Atkinson C. On stress singularities and interfaces in linear elastic fracture mechanics. Int J Fract 1977;13(6):807–20.

[26] Sorensen L, Botsis J, Gmür Th, Humbert L. Bridging tractions in Mode I delamination: measurements and simulations. Compos Sci Technol 2008;68(12):2350–8.
[27] Shahverdi M, Vassilopoulos AP, Keller T. Modeling effects of asymmetry and fiber bridging on Mode I fracture behavior of bonded pultruded composite joints. Engng Fract Mech 2013;99:335–48.
[28] de Morais AB. A new fibre bridging based analysis of the Double Cantilever Beam (DCB) test. Composite Part A 2011;42(10):1361–8.
[29] Tamuzs V, Tarasovs S, Vilks U. Progressive delamination and fiber bridging modeling in double cantilever beam composite specimens. Engng Fract Mech 2001;68(5):513–25.
[30] Sørensen BF, Jacobsen TK. Characterizing delamination of fibre composites by mixed mode cohesive laws. Compos Sci Technol 2009;69(3–4):445–56.
[31] ASTM D3039/D3039M-08 Standard test method for tensile properties of polymer matrix composite materials. In: Annual book of ASTM standards: adhesive section 15.06.
[32] ASTM D5573–99(2005): Standard practice for classifying failure modes in fiber-reinforced-plastic (FRP) joints. In: Annual book of ASTM standards: 15.06.
[33] De Castro J, Keller T. Ductile double-lap joints from brittle GFRP laminates and ductile adhesives. Part I: Experimental investigation. Composite Part B-Engineering 2008;39(2):271–81.
[34] ASTM D3171–11: Standard test methods for constituent content of composite materials. In: Annual book of ASTM standards: adhesive section 15.03.
[35] Xu XP, Needleman A. Numerical simulations of fast crack growth in brittle solids. J Mech Phys Solids 1994;42(9):1397–434.
[36] ANSYS mechanical APDL structural analysis guide. Release 13.0; November 2010. <http://www1.ansys.com/customer/content/documentation/130/ans_str.pdf>.